

RESEARCH ARTICLE | AUGUST 25 2023

Molecular dynamics simulation study on the mass transfer across vapor–liquid interfaces in azeotropic mixtures

Vilde Bråten ; Dominik Schaefer ; Simon Stephan  ; Hans Hasse 

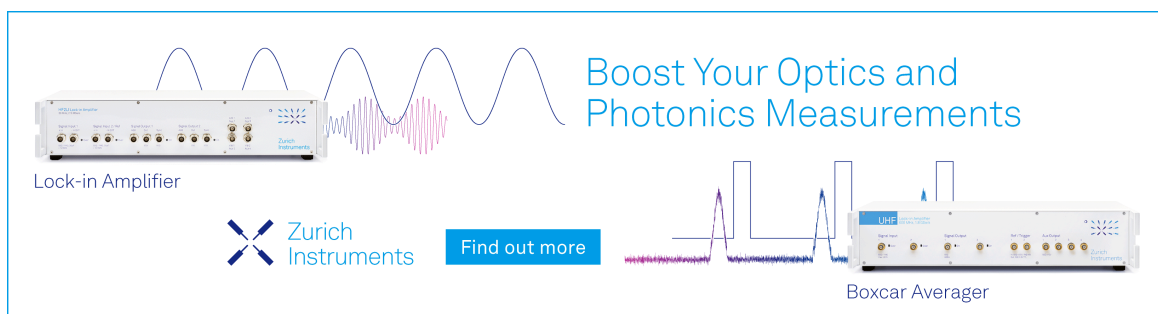


J. Chem. Phys. 159, 084503 (2023)

<https://doi.org/10.1063/5.0165421>



29 April 2024 12:53:28



Boost Your Optics and Photonics Measurements

Lock-in Amplifier

Zurich Instruments

Find out more

Boxcar Averager

Molecular dynamics simulation study on the mass transfer across vapor–liquid interfaces in azeotropic mixtures

Cite as: *J. Chem. Phys.* **159**, 084503 (2023); doi: [10.1063/5.0165421](https://doi.org/10.1063/5.0165421)

Submitted: 28 June 2023 • Accepted: 24 July 2023 •

Published Online: 25 August 2023



View Online



Export Citation



CrossMark

Vilde Bråten,  Dominik Schaefer,  Simon Stephan,^{a)}  and Hans Hasse 

AFFILIATIONS

Laboratory of Engineering Thermodynamics (LTD), RPTU Kaiserslautern, Kaiserslautern, Germany

^{a)} Author to whom correspondence should be addressed: simon.stephan@rptu.de

ABSTRACT

Mass transfer through fluid interfaces is an important phenomenon in industrial applications as well as in naturally occurring processes. In this work, we investigate the mass transfer across vapor–liquid interfaces in binary mixtures using molecular dynamics simulations. We investigate the influence of interfacial properties on mass transfer by studying three binary azeotropic mixtures known to have different interfacial behaviors. Emphasis is placed on the effect of the intermolecular interactions by choosing mixtures with the same pure components but different cross-interactions such that different azeotropic behaviors are obtained. The molar flux is created by utilizing a non-stationary molecular dynamics simulation approach, where particles of one component are inserted into the vapor phase over a short period of time before the system's response to this insertion is monitored. From a direct comparison of the density profiles and the flux profiles in close proximity to the interface, we analyze the particles' tendency to accumulate in the interfacial region throughout the different stages of the simulation. We find that for mixtures with strong attractive cross-interactions, the inserted particles are efficiently transported into the liquid phase. For systems with weak attractive cross-interactions, the inserted particles show a tendency to accumulate in the interfacial region, and the flux through the system is lower. The results from this work indicate that the accumulation of particles at the interface can act as a hindrance to mass transfer, which has practical relevance in technical processes.

© 2023 Author(s). All article content, except where otherwise noted, is licensed under a Creative Commons Attribution (CC BY) license (<http://creativecommons.org/licenses/by/4.0/>). <https://doi.org/10.1063/5.0165421>

I. INTRODUCTION

The properties of fluid interfaces play important roles in various processes such as nucleation,^{1,2} wetting,^{3,4} and evaporation and condensation.^{5,6} The presence of vapor–liquid and liquid–liquid interfaces can also affect the operating conditions of industrial applications such as natural gas production,^{7–9} enhanced oil recovery,¹⁰ and carbon dioxide sequestration.^{11,12} Acquiring good knowledge on a system's interfacial properties and how they affect a process is therefore of considerable interest.^{13–16} Macroscopically, interfaces are usually treated as two-dimensional objects, while in reality, their thickness spans over a few nanometers. Within the interfacial region, interesting changes in the system's thermodynamic and structural behavior can occur. In two-phase fluid mixtures, a higher specific configuration of the surface excess of one component can lead to a non-monotonic density profile across the interface.^{17–23} This feature is referred to as enrichment and can prompt the formation of a

wetting thin film at the interface that can be interpreted as a precursor for a second liquid phase.^{15,17}

The features of mixtures' interfaces can also affect the mass transfer in the system. Multiple studies have suggested that enrichment can influence mass transfer.^{13,18,24–28} To investigate this relation, we recently developed a non-stationary, non-equilibrium molecular dynamics (NEMD) simulation method.²⁸ The method is utilized in this work to systematically study mass transfer across fluid interfaces of different mixtures at different thermodynamic conditions. The investigated simulation box contains a vapor phase in contact with a liquid phase that is crossing the periodic boundary (cf. Fig. 1). The non-stationary molar flux is introduced by appropriately prescribing the chemical potential in a control volume (CV) in the middle of the vapor phase. This leads to an insertion of particles over a short period of time, i.e., in a pulse-like manner. The method has previously been applied to two binary mixtures of particles interacting through the Lennard–Jones truncated and shifted

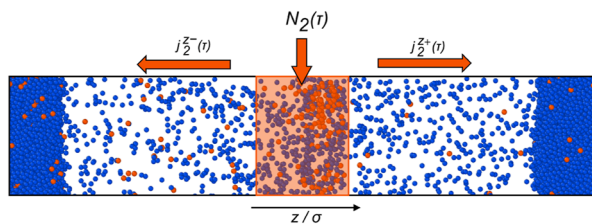


FIG. 1. Illustration of the simulation method. During the insertion interval, the orange particles are inserted into the control volume marked by the orange shaded area. Following the insertion interval, the orange particles spread through the vapor phase, cross the vapor-liquid interface, and enter the liquid phase.

(LJTS) potential, where the first mixture is known to exhibit a strong enrichment of the low-boiling component while the second mixture shows no enrichment.^{15,16,20,27–29} Even though both mixtures have similar transport coefficients in the bulk phases, the observed mass transfers differ significantly. This indicates that there is a connection between the enrichment and the mass transfer. However, the vapor–liquid interfaces of mixtures are not only characterized by the enrichment but also by the thickness of the interface, the surface tension, and the relative adsorption.^{15,20,30} All the interfacial properties are related, and this relation is mixture-dependent. Isolating the influence of only one interfacial property on mass transfer can therefore be challenging. In this work, we aim to further elucidate the connection between the various interfacial properties and the mass transfer by applying the NEMD method from Ref. 28 to binary azeotropic LJTS mixtures. The phase equilibrium and equilibrium interfacial properties of these mixtures are available from the comprehensive study performed by Staubach and Stephan.³⁰

The behavior of an azeotropic mixture depends strongly on the cross-interactions of its constituents.³¹ When the attractive cross-interactions are stronger than the interactions between the pure components, the mixture usually has a high-boiling azeotrope. In contrast, when the attractive cross-interactions are weaker than the interactions between the pure components, the mixture typically has a low-boiling azeotrope. For very weak attractive cross-interactions, a hetero-azeotrope can occur, which is a liquid–liquid de-mixing in conjunction with an azeotrope. We investigate one mixture from each category. The mixtures all consist of the same two pure components but differ in their cross-interactions. This allows us to isolate the effect of the cross-interactions and analyze how they influence the mass transfer in the system. Another interesting aspect of azeotropic mixtures is their phase diagrams, where the relative volatility of the components can be changed by varying the mixture's mole fraction. This represents a special feature for the enrichment in azeotropic mixtures since the enriching component changes at the azeotropic point, i.e., in each azeotropic branch, the respective low-boiling component exhibits enrichment.^{30,32} Additionally, the relative adsorption, the interfacial thickness, and the surface tension show distinct behaviors in azeotropic mixtures.³⁰

In previous work,²⁸ the non-stationary method was only applied to systems that consisted only of the high-boiling component prior to the insertion of the low-boiling component. In this work, we have extended the simulation technique by investigating systems that were binary mixtures before insertion. This more

closely resembles the operating conditions of industrial processes, which rarely start from pure systems. Starting from a binary mixture also allows us to study the system under a wider range of conditions and investigate whether the mass transfer of one component is significantly hindered by the enrichment of another component.

II. METHODS

In the following sections, we present the simulation setup and the sampling techniques utilized to investigate the mass transfer in the azeotropic systems. Since the simulation method is presented in detail in Ref. 28, we only present a brief outline of the method here (cf. Sec. II A). The three studied binary LJTS mixtures are introduced in Sec. II B.

A. Simulation method

The molecular dynamics (MD) simulations were performed with the simulation package *ls1*.³³ The investigated setup consists of a vapor phase in contact with a liquid phase that crosses the periodic boundary of the simulation box, as illustrated in Fig. 1. Consequently, there are two vapor–liquid interfaces present in the system. The z -coordinate is defined such that it is orthogonal to the planar vapor–liquid interfaces. The simulation run can be divided into five intervals. The first interval is referred to as the initial equilibration interval (*IniEq*), in which the system evolves from its initial configuration into the first vapor–liquid equilibrium state. The properties of this first vapor–liquid equilibrium state are sampled during the second interval, which is called *Eq1*. The third interval is the insertion interval (*In*), in which particles of one component type are inserted in the middle of the vapor phase; cf. Fig. 1. The particle insertion is controlled by a Monte Carlo algorithm that adjusts the number of particles in a CV based on a prescribed chemical potential, $\mu_{i,CV}$, where i refers to the particle type. After the insertion interval follows the relaxation interval (*Relax*), in which the system's response to the particle insertion is monitored and evaluated. The *Relax* interval is of prime interest here. The final interval is used to sample the second vapor–liquid equilibrium state (*Eq2*). In the following, the abbreviations given in brackets are used when referring to the different intervals.

During the simulations, several observables are sampled as a function of time τ and the z -coordinate. The z -positions are discretized into 1200 bins. The sampled observables are the pressure tensor p , the density of the individual components ρ_i , the molar composition x_i , and the rate of change of the density with respect to time $\partial\rho_i/\partial\tau$. The values of $\partial\rho_i/\partial\tau$ are determined by numerical differentiation of the local density with respect to time. The molar flux of component i j_i is computed from the molar balance. The molar balance of bin n at time step τ can be written as

$$\frac{\partial\rho_i}{\partial\tau}(\tau, n) = -\frac{j_i(\tau, n+1) - j_i(\tau, n)}{\Delta z_{\text{bin}}}, \quad (1)$$

where $j_i(\tau, n+1)$ and $j_i(\tau, n)$ are the fluxes through the left and right bin boundaries, respectively, while Δz_{bin} is the bin size. In this work, j_i represents the net molar flux. In order to solve Eq. (1) for the entire system, the symmetry boundary condition is applied, i.e., the net flux in the middle of the liquid slab is zero. The technique utilized to determine the symmetry plane is described below.

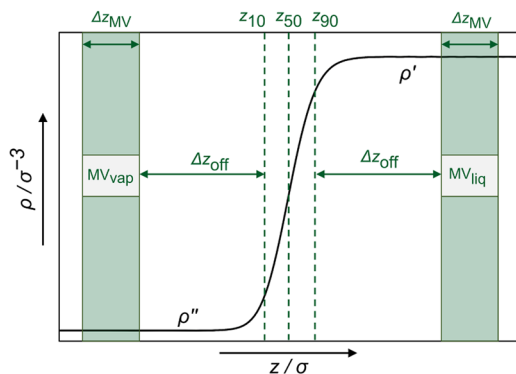


FIG. 2. Schematic of the positions of the measurement volumes (MVs) relative to the location of the interface. The positions z_{10} , z_{50} , and z_{90} are defined by Eqs. (2)–(4). MV_{vap} and MV_{liq} are located at a distance $\Delta z_{\text{off}} = 7\sigma$ from the positions z_{10} and z_{90} , respectively. The width of each MV is $\Delta z_{\text{MV}} = 1\sigma$.

Due to the adsorption of the inserted component, the location of the vapor–liquid interfaces fluctuates during the simulation. For the two interfacial regions, we define three different positions: $z_{10} = z(\rho_{10})$, $z_{50} = z(\rho_{50})$, and $z_{90} = z(\rho_{90})$, corresponding to the location for which the local total density equals ρ_{10} , ρ_{50} , and ρ_{90} , respectively (cf. Fig. 2). The densities ρ_{10} , ρ_{50} , and ρ_{90} are defined by

$$\rho_{10} = \rho'' + 0.1(\rho' - \rho''), \quad (2)$$

$$\rho_{50} = \rho'' + 0.5(\rho' - \rho''), \quad (3)$$

$$\rho_{90} = \rho'' + 0.9(\rho' - \rho''), \quad (4)$$

where ρ'' is the total density in the bulk vapor phase and ρ' is the total density in the bulk liquid phase. The symmetry plane is defined as the midpoint between z_{50} of the right interface and z_{50} of the left interface. In the evaluation of the results, we focus on the right interface, such that a positive flux is directed toward the interface and a negative flux is directed away from the interface.

The behavior of the system in the vicinity of the vapor–liquid interface is of particular interest. We, therefore, sample the system's properties in measurement volumes (MVs) close to the interface. The MVs on the vapor and liquid side are referred to as MV_{vap} and MV_{liq} , respectively, and their positions are defined with respect to the interface position as illustrated in Fig. 2.

For non-stationary systems investigated by MD simulations, a common strategy for reducing the signal-to-noise ratio is to perform simulations of replicas of the system starting from different initial configurations.^{34–36} In this work, we carried out 100 replicas for all simulations. The replicas differ only in their initial velocity distributions. The presented results were obtained by averaging over the left and right interfaces and over the 100 individual replicas. The errors were computed from the standard deviation of the replicas. Details on the settings applied for the different simulations are presented in the supplementary material.

B. Azeotropic binary Lennard–Jones mixtures

The three studied Lennard–Jones (LJ) systems are named mixtures A, B, and C. The interactions were modeled using the LJTS potential with a cut-off radius of $r_c = 2.5\sigma$. In the following, all properties are presented in reduced LJ units with respect to the LJ potential parameters of component 1 and the Boltzmann constant, k_B .³⁷ For all the mixtures investigated in this work, the size parameter σ_i and the mass m_i were equal and set to unity for both components. The energy parameter of component 1 was also set to unity, while we applied $\varepsilon_2/\varepsilon_1 = 0.9$ for component 2. These values remained unchanged for the three investigated mixtures. The cross-interactions were modeled by the modified Lorentz–Berthelot^{38,39} combination rules:

$$\sigma_{12} = \frac{\sigma_1 + \sigma_2}{2}, \quad (5)$$

$$\varepsilon_{12} = \xi_{12} \sqrt{\varepsilon_1 \varepsilon_2}, \quad (6)$$

where ξ_{12} is the binary interaction parameter. Since the values of ε_1 and ε_2 are the same for all investigated mixtures, the mixtures only differ in ξ_{12} . We chose three different values of ξ_{12} , resulting in three azeotropic mixtures. All mixtures were investigated at four temperatures: $T = 0.660 \varepsilon k_B^{-1}$, $T = 0.715 \varepsilon k_B^{-1}$, $T = 0.770 \varepsilon k_B^{-1}$, and $T = 0.825 \varepsilon k_B^{-1}$. Mixture A, with $\xi_{12} = 0.8$, is a hetero-azeotrope for the three lowest temperatures, while it is a low-boiling azeotrope for the highest temperature. Mixture B, with $\xi_{12} = 0.9$, is a low-boiling azeotrope, and mixture C, with $\xi_{12} = 1.2$, is a high-boiling azeotrope.

Since the bulk and interfacial properties of these mixtures have previously been systematically studied by our group,³⁰ the results from the NEMD simulations can be put in the context with the corresponding equilibrium properties. The hetero-azeotrope and the low-boiling azeotrope show enrichment of the low-boiling component, while the high-boiling azeotrope shows no enrichment. Moreover, the enrichment decreases with increasing temperature and increasing mole fraction of the low-boiling component. The surface tension also decreases with increasing temperature. At a given temperature and composition, the surface tension increases with increasing cross-interactions. For all three mixtures, the relative adsorption $\Gamma_i^{(j)}$ is zero under three conditions: at infinite dilution of component i , at extremum in the surface tension isotherm, or at the mixtures' critical point. In addition, common to all three mixtures is that the interfacial thickness increases with increasing temperature.

The thermophysical properties of various LJTS mixtures have been found to be accurately represented by the PeTS equation of state (EoS).^{15,16,19,20,30,40–42} Deviations between the MD simulation results and the EoS predictions were only observed in the direct vicinity of the critical points. In particular, for mixture A, this systematic deviation was found to increase with temperature.³⁰ Figure 3 shows the mixtures' pressure–composition phase diagrams predicted by the PeTS EoS. For all mixtures at all temperatures, we investigated how systems consisting only of component 1 responded to the insertion of component 2 (filled circles in Fig. 3). In addition, we investigated two different initial compositions of mixture A at temperature $T = 0.715 \varepsilon k_B^{-1}$: one on the right side of the azeotropic point where component 2 is the low-boiling component (filled squares in

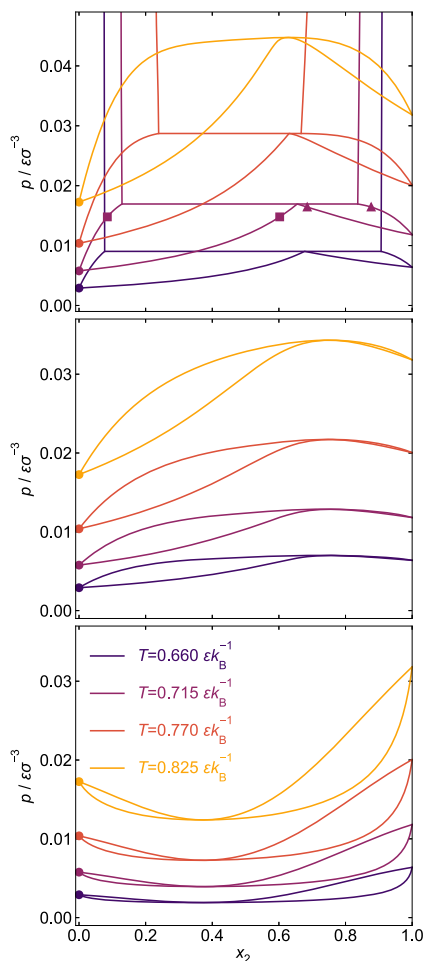


FIG. 3. Pressure-composition phase diagram of the studied mixtures at the four studied temperatures calculated with the PeTS EoS: (top) mixture A, (middle) mixture B, and (bottom) mixture C. The predicted starting configurations for the different simulations are illustrated by markers: circles represent pure component 1, squares represent composition α , and triangles represent composition β .

Fig. 3, referred to as composition α), and one on the left side of the azeotropic point where component 1 is the low-boiling component (filled triangles in Fig. 3, referred to as composition β). Starting from these compositions, we performed two different simulations: one where component 2 was inserted (referred to as α_2 and β_2) and one where component 1 was inserted (referred to as α_1 and β_1).

In total, the influence of four different variables on the results was investigated: the cross-interactions, the temperature, the composition, and the identity of the inserted component, which resulted in 16 different simulations. For convenience, we refer to the individual simulations as $X_T^{i,\chi}$, where X refers to the mixture name (A, B, or C), T to the temperature, i to the identity of the inserted component, and χ to the composition of the initial state (α or β). For the simulations starting from pure component 1, we use $\chi = p$.

III. RESULTS AND DISCUSSION

In the following, we present the heterogeneous systems' response to the introduced flux and analyze the connection between interfacial properties and mass transfer. Sections III A and III B contain the results for the systems starting from pure states, while Sec. III C contains the results for the systems starting from mixture states. We utilize two different approaches for characterizing the interfacial properties and the fluxes. The first approach involves an investigation of the time evolution of the properties sampled in MV_{vap} and MV_{liq} . The temperature dependence of this time evolution for mixture A is presented in Sec. III A. The second approach is a direct comparison of the density profiles to the flux profiles in close proximity to the interface. The results of this approach are presented in Sec. III B for the three different mixtures at $T = 0.715 \epsilon k_B^{-1}$. For the systems starting from mixture states, we present the results of the second approach in Sec. III C. All remaining combinations of mixtures, temperatures, and initial states are presented in the supplementary material.

A. Influence of temperature on mass transfer

The results for mixture A at the four investigated temperatures ($A_{0.660}^{2,p}$, $A_{0.715}^{2,p}$, $A_{0.770}^{2,p}$, and $A_{0.825}^{2,p}$) are presented in Fig. 4. The time evolution of the density, flux, and pressure sampled in the MVs is depicted. Figures 4(a) and 4(b) show that ρ_2'' increases with increasing temperature, while ρ_2' decreases with increasing temperatures. This is a consequence of the temperature dependence of the solubility of component 2 in component 1. The insertion of particles imposes a flux in the vapor phase directed toward the interface. Figures 4(c) and 4(d) show the flux measured at the positions $z = z_{10} - 7\sigma$ and $z = z_{90} + 7\sigma$. At all temperatures, a prominent peak is observed on the vapor side shortly after the insertion of particles. The peak stems from the arrival of the vast majority of the inserted particles. The differences in the flux for the different temperatures are mainly limited to this peak; the height of the peak increases with decreasing temperature, which can be attributed to the increased solubility of component 2 at lower temperatures. On the liquid side, no significant temperature dependence of the flux is observed due to the low signal-to-noise ratio. Figures 4(e) and 4(f) show that the pressure is the same in MV_{vap} and MV_{liq} —both at the beginning and end of the process. The pressure reaches its equilibrium value quicker than the density, which indicates that mechanical equilibrium is established quickly. The large fluctuations of the liquid phase pressure are a well-known phenomenon, attributed to the sensitivity of the measurement of this property.^{28,43,44} For all presented properties, the change in temperature leads to quantitative changes, but the qualitative behavior of the properties remains unchanged. Similar observations were made for mixtures B and C. For details, see the supplementary material.

B. Influence of mixture behavior on mass transfer

The density and flux profiles for the three mixtures at temperature $T = 0.715 \epsilon k_B^{-1}$ ($A_{0.715}^{2,p}$, $B_{0.715}^{2,p}$ and $C_{0.715}^{2,p}$) are presented in Fig. 5. In the following, we compare how the ρ_2 - and j_2 -profiles evolve with time for the different mixtures. Since the In interval starts at $\tau = 1,000 \sigma(m/\epsilon)^{1/2}$, all profiles measured before this time represent the equilibrium state of pure component 1 ($Eq1$). The

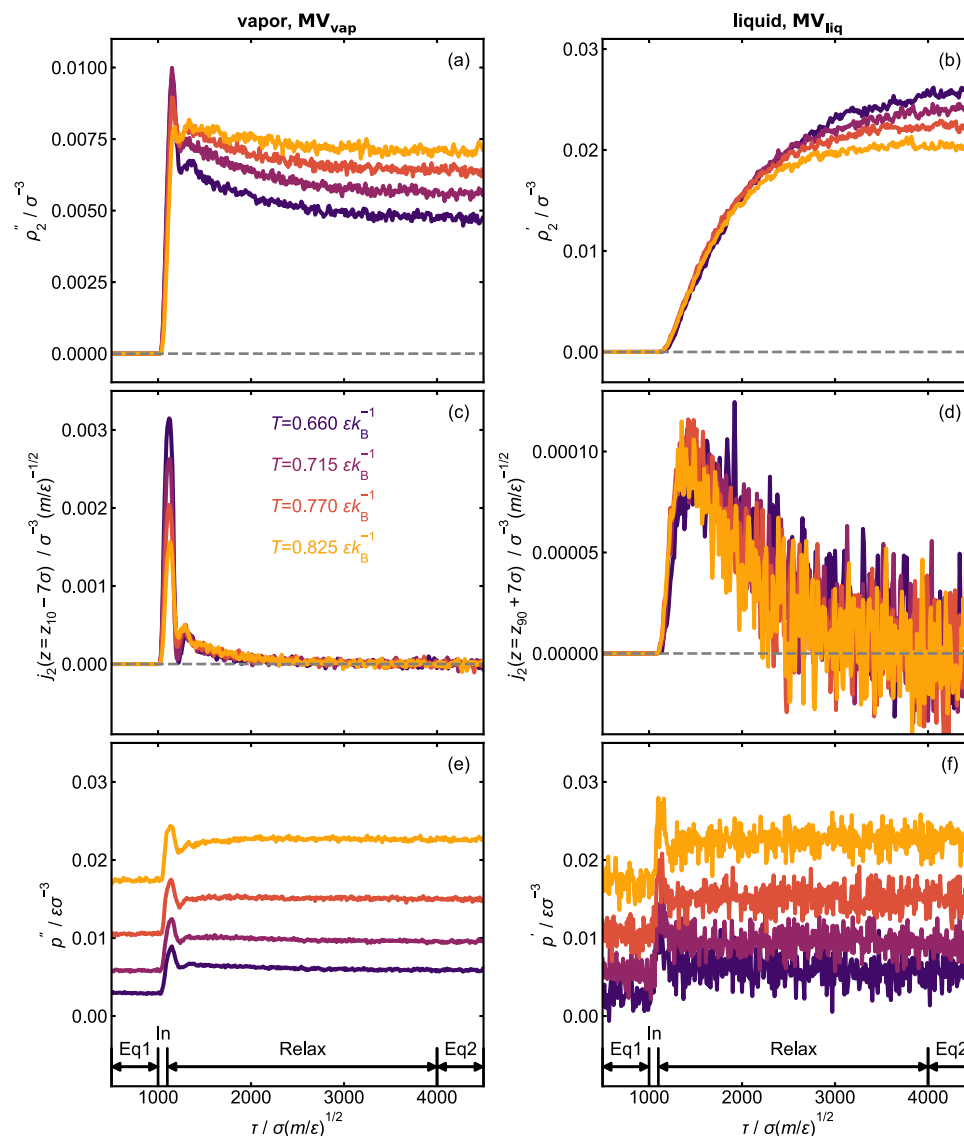


FIG. 4. Results from the simulations starting from the pure component 1 for mixture A at the four studied temperatures. Results obtained in MV_{vap} are shown on the left side, while those obtained in MV_{liq} are shown on the right side. Top: density of component 2, middle: flux of component 2, and bottom: pressure. The different intervals of the simulation are indicated on the time axis.

Relax interval starts at $\tau = 1,100 \sigma(m/\epsilon)^{1/2}$. At the beginning of the *Relax* interval, the concentration of component 2 in the interfacial region is low because the inserted particles have not reached this region yet. Hence, the properties of the interface are mainly governed by the behavior of component 1. As a consequence, the profiles of ρ_2 and j_2 at the beginning of the *Relax* interval are similar for the different mixtures. The ρ_2 -profiles show a small peak close to the interfacial position, and the corresponding flux profiles (indicated by arrows in Fig. 5) show that the insertion of particles imposes a flux in the vapor phase directed toward the interface.

Since the friction in the vapor phase is low, the particles reach the interface with a high directed velocity. At the point of the interface, the flux profiles decay quickly due to the higher density of the liquid phase.

As the system evolves through the *Relax* interval, important differences between the mixtures become apparent. Common for all mixtures is that the absolute height of the density peak increases, with ongoing simulation time before it decays toward the equilibrium profile of the mixture (*Eq2*). This indicates that more particles arrive at the interface than are further transported into the liquid

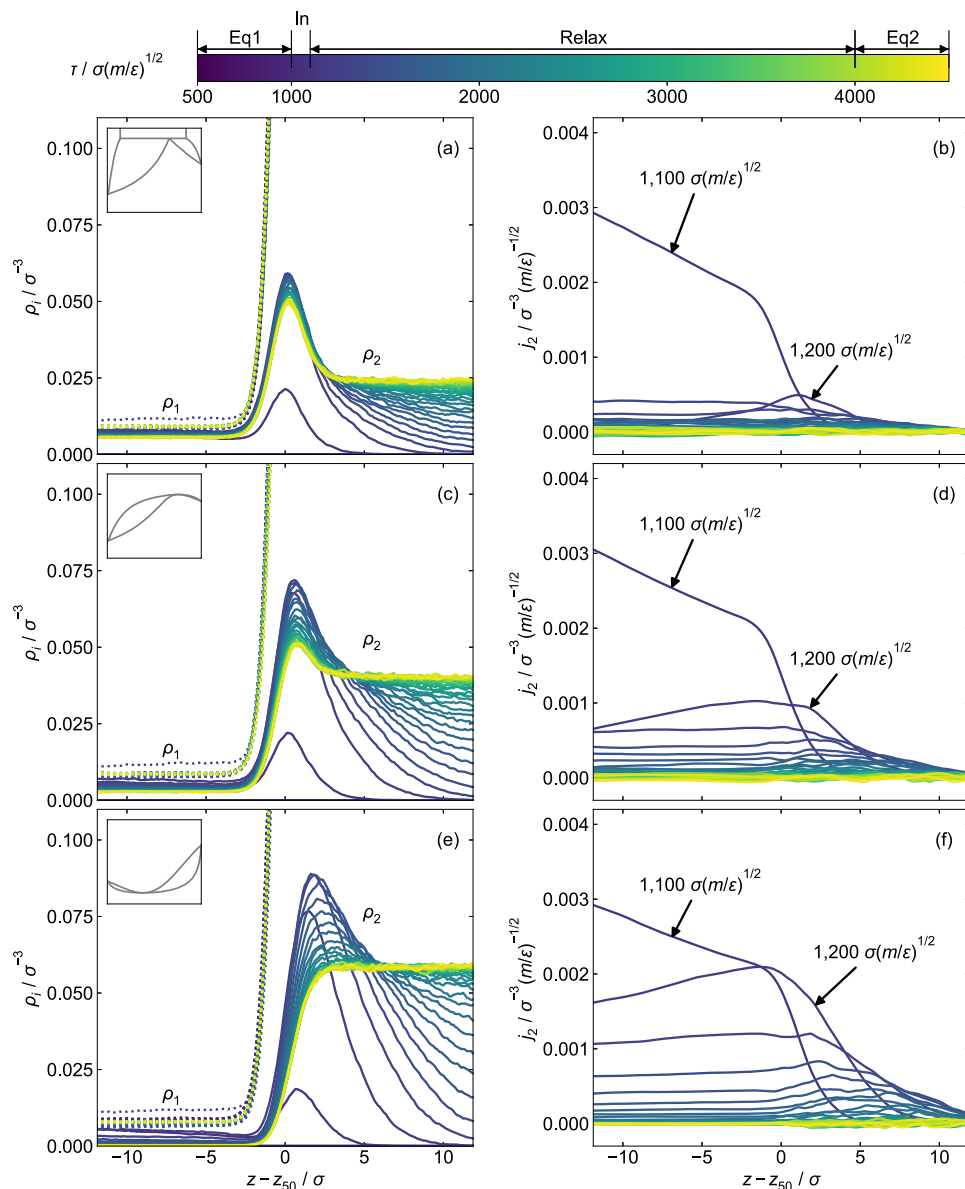


FIG. 5. Density and flux profiles in the region close to the interface as a function of the z -coordinate. The results are displayed in (a) and (b) for mixture A, (c) and (d) for mixture B, and (e) and (f) for mixture C. The interface is located at $z - z_{50} = 0$. The simulation time is indicated by color, and the profiles are displayed at intervals of $\delta\tau = 100 \sigma(m/\epsilon)^{1/2}$. The temperature is $T = 0.715 \epsilon k_B^{-1}$. The inset shows the phase diagram predicted from the PeTS EoS.

phase. However, there are significant differences: with increasing ξ_{12} , the height of the temporary density peak increases and the position of the peak is shifted further into the liquid phase. This indicates that for higher values of ξ_{12} , the particles of component 2 are transported more efficiently into the liquid phase. This is also reflected by the flux profiles [Figs. 5(b), 5(d), and 5(f)], which show that higher values of ξ_{12} result in an increased ability to maintain a higher flux in both the vapor and the liquid phases. At

$\tau = 1,200 \sigma(m/\epsilon)^{1/2}$, we observe that going from mixture A to mixture B to mixture C, the flux increases each time approximately by a factor of two. The correlation between the flux and ξ_{12} is supported by the fact that the relative adsorption of component 2 at the interface decreases with increasing ξ_{12} .³⁰ Accordingly, with increasing ξ_{12} , the particles have an increased tendency toward preferential residency in the liquid phase than in the interfacial region.

In the final equilibrium state of the mixtures (*Eq2*), displayed by the yellow lines in Fig. 5, the ρ_2 -profiles show enrichment for $A_{0.715}^{2,p}$ and $B_{0.715}^{2,p}$, while there is no enrichment for $C_{0.715}^{2,p}$. This behavior is in accordance with the equilibrium properties reported in Ref. 30. The difference in the density profiles of the *Eq2* state suggests that the buildup of the temporary density peaks at the beginning of the *Relax* interval is caused by different processes. These differences were analyzed in detail in a previous paper from our group.²⁸ While the density peaks observed at the beginning of the *Relax* interval for $A_{0.715}^{2,p}$ and $B_{0.715}^{2,p}$ can be attributed to the tendency of the low-boiling component to accumulate in the interfacial region; this is not the case for $C_{0.715}^{2,p}$. For the latter system type, the temporary density peak is rather interpreted as a type of jamming; since the transport of the inserted particles in the liquid phase is diffusion-controlled and slower than the transport in the vapor phase, we get an accumulation of the particles in the interfacial region. This accumulation disappears over time as the particles move further into the liquid phase.

Since the temporary density peaks for mixtures A and B are higher than those of the *Eq2* state, the buildup of the temporary density peak is probably caused by a combination of enrichment and jamming. For $C_{0.715}^{2,p}$, which has zero enrichment in the *Eq2* state, the temporary density peak is purely caused by the jamming effect. In the work by Schaefer *et al.*,²⁸ it was suggested that the temporary density peak in mixtures without enrichment can be caused by a higher solubility due to increased pressure. This argument does not hold for mixture C in this work since the bubble line has a negative slope for the compositional range investigated here (cf. Fig. 3). In Ref. 28, a temporarily negative flux in the vapor phase was reported, i.e., a net repelling of component 2 particles from the interface. This was not observed for any of the mixtures and states investigated here.

C. Inserting particles into a mixture

In this section, we present the results of the simulations where particles are inserted into a system where both components of mixture A are already present. This corresponds to the simulations $A_{0.715}^{2,\alpha}$, $A_{0.715}^{2,\beta}$, $A_{0.715}^{1,\alpha}$, and $A_{0.715}^{1,\beta}$. For composition α , component 2 is the low-boiling component, while for composition β , component 1 is the low-boiling component. To clearly illustrate how the systems are evolving over time, Fig. 6 shows the properties sampled in the MVs in a pressure-composition diagram along with the PeTS EoS prediction of the dew and the bubble line. To reduce the signal-to-noise ratio of the pressure, moving average smoothing was applied to the data. Figure 6(a) shows the results of inserting component 2 ($A_{0.715}^{2,\alpha}$ and $A_{0.715}^{2,\beta}$) while Fig. 6(b) shows the results of inserting component 1 ($A_{0.715}^{1,\alpha}$ and $A_{0.715}^{1,\beta}$). Similarly to the results presented in Sec. III A, the pressure sampled in the MVs increases directly after the insertion of particles before it quickly reaches the equilibrium value. For all investigated systems, the PeTS EoS prediction for the liquid phase pressure slightly deviates from the simulation results. This has been reported before for highly non-ideal systems with positive deviations from Raoult's law.^{15,20,30}

The density and flux profiles obtained from the insertion of component 2 are shown in Fig. 7, while the profiles obtained from

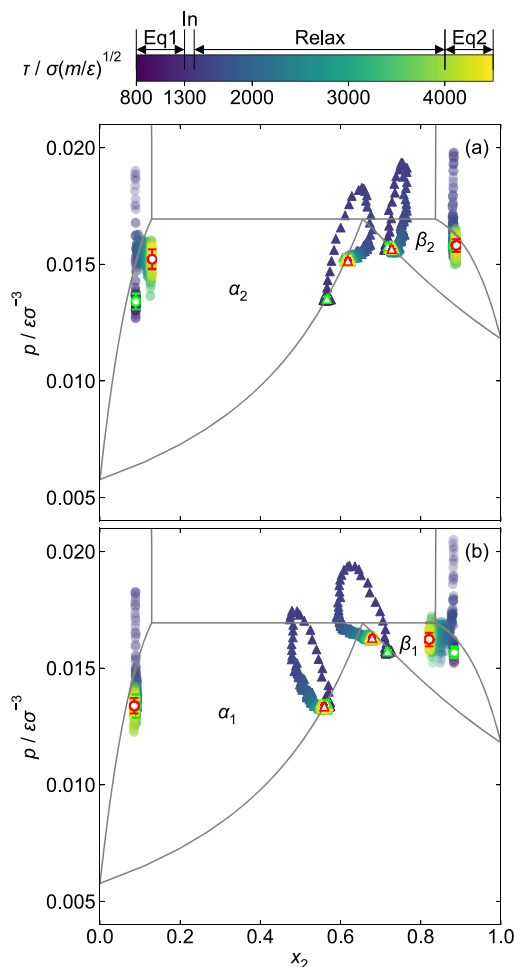


FIG. 6. Phase diagram for mixture A at $T = 0.715 \epsilon k_B^{-1}$ predicted by the PeTS EoS (gray lines). Triangles and circles indicate properties sampled in MV_{vap} and MV_{liq} , respectively: (a) insertion of component 2 and (b) insertion of component 1. The bright green and red markers indicate the time averages of the states sampled during the intervals in *Eq1* and *Eq2*, respectively. The error bars represent two standard deviations.

the insertion of component 1 are shown in Fig. 8. Simulations $A_{0.715}^{2,\alpha}$ and $A_{0.715}^{1,\beta}$ [Figs. 7(a) and 8(c)] both represent insertion of the low-boiling component and can, therefore, be directly compared to simulation $A_{0.715}^{2,p}$ [Fig. 5(a)]. Common for these three simulations is that the absolute height of the density peak first increases as the simulation time increases before it decays toward the equilibrium profile of the *Eq2* state. This indicates that the jamming of the particles at the interface occurs irrespective of the composition of the *Eq1* state. Simulations $A_{0.715}^{1,\alpha}$ and $A_{0.715}^{2,\beta}$ [Figs. 7(c) and 8(a)] represent the insertion of the high-boiling component, which leads to a decrease in the density peak of the low-boiling component. This is in accordance with the behavior of the enrichment at equilibrium states for these systems.³⁰

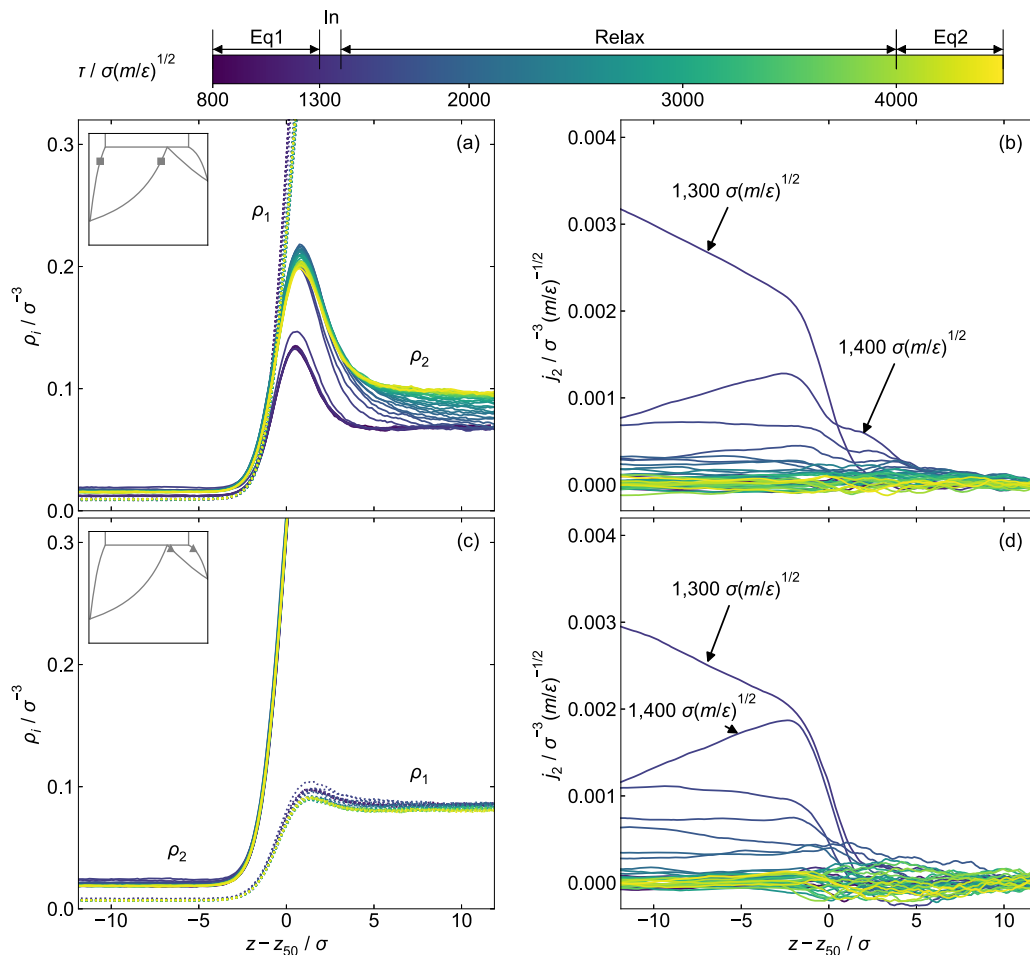


FIG. 7. Density and flux profiles in the region close to the interface after insertion of component 2, as a function of the z -coordinate, (a) and (b) for composition α , (c) and (d) for composition β . The interface is located at $z - z_{50} = 0$. Each line displays a profile at a given time step. The profiles are displayed at intervals of $\delta\tau = 100 \sigma(m/\epsilon)^{1/2}$. The temperature is $T = 0.715 \epsilon k_B^{-1}$. The inset shows the phase diagram predicted from the PeTS EoS with the indicated starting configuration.

The fluxes at the beginning of the *Relax* interval are influenced by the vapor phase density in the *Eq1* state, which is higher for β than for α . This explains why the flux profile directly after insertion ($\tau = 1,300 \sigma(m/\epsilon)^{1/2}$) is larger for the systems starting from composition α than for those starting from composition β .

The most interesting fluxes to compare are those corresponding to the same starting compositions but with different identities of the inserted particles, i.e., comparing simulation $A_{0.715}^{1,\alpha}$ to $A_{0.715}^{2,\alpha}$ and $A_{0.715}^{1,\beta}$ to $A_{0.715}^{2,\beta}$. When the low-boiling component 2 is inserted into composition α [Fig. 7(b)], the flux profiles decay quickly over time, similar to the observations made for simulation $A_{0.715}^{2,p}$. In contrast, when the high-boiling component 1 is inserted into composition α [Fig. 8(b)], the flux remains non-zero for more than half of the

Relax interval. Similarly, for the simulations starting from composition β , the flux decays more quickly with time after insertion of the low-boiling component 1 [Fig. 8(d)] than after insertion of the high-boiling component 2 [Fig. 7(d)]. This indicates that the mass transfer of one component is not significantly hindered by the enrichment of another component.

One unique feature is observed for simulation $A_{0.715}^{2,\alpha}$ [cf. Fig. 7(b)] where the flux profile displays a double hump at time $\tau = 1,400 \sigma(m/\epsilon)^{1/2}$. We interpret the hump on the vapor side as an effect of the buildup of the peak of the density profile, while the hump on the liquid side is due to the rush of the particles into the liquid phase. For simulation $A_{0.715}^{1,\beta}$ [cf. Fig. 8(d)], no double hump is observed during the buildup of the enrichment, which probably can be attributed to the low enrichment for this state.

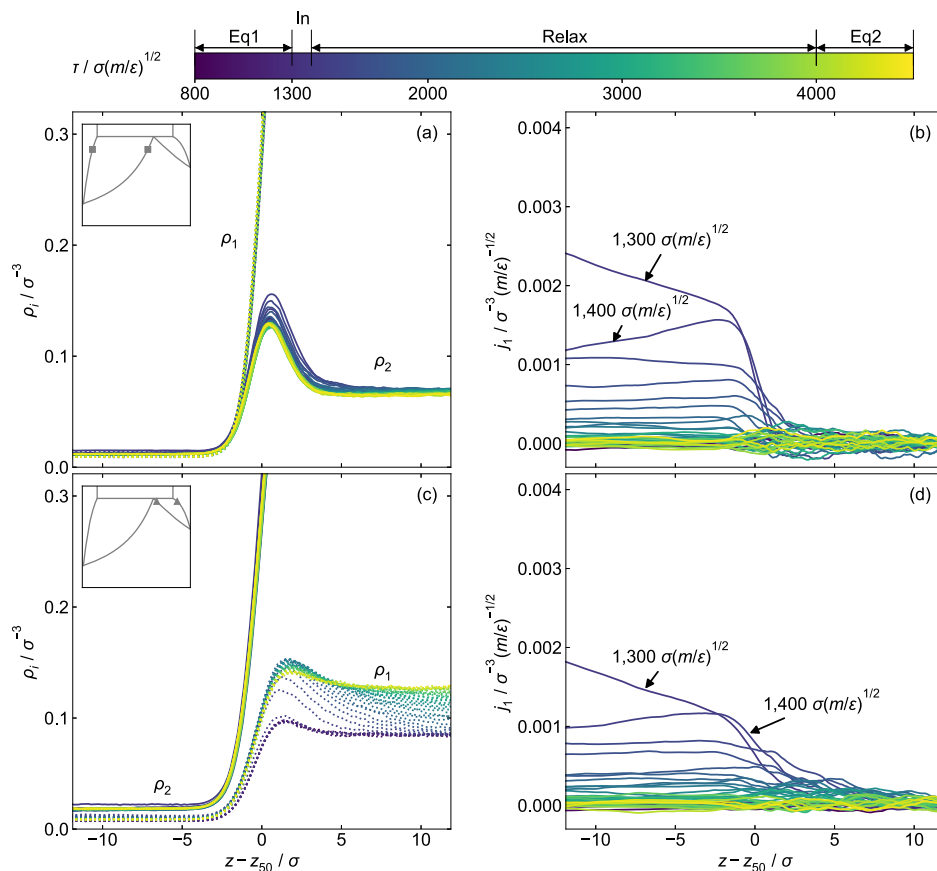


FIG. 8. Density and flux profiles in the region close to the interface after insertion of component 1, as a function of the z -coordinate, (a) and (b) for composition α , (c) and (d) for composition β . The interface is located at $z - z_{50} = 0$. Each line displays a profile at a given time step. The profiles are displayed at intervals of $\delta\tau = 100 \sigma(m/\epsilon)^{1/2}$. The temperature is $T = 0.715 \epsilon k_B^{-1}$. The inset shows the phase diagram predicted from the PeTS EoS with the indicated starting configuration.

IV. CONCLUSIONS

We have investigated the connection between interfacial properties and mass transfer for three binary azeotropic mixtures of LJTS particles. The mixtures all have the same pure components but different cross-interactions, which leads to important differences in their interfacial properties. The systems were investigated using the non-stationary NEMD simulation procedure presented in previous work by our group,²⁸ where particles of one component are inserted into a vapor–liquid equilibrium system. In all studied simulations, the number of inserted particles was approximately the same. Yet, important differences in the time evolution of the density and flux profiles are observed. These differences are attributed to differences in interfacial properties such as enrichment, surface tension, and relative adsorption. We also investigated how the connection between the interfacial properties and mass transfer depends on temperature, composition, and the volatility of the inserted component. The results provide new insights into the physical processes of vapor–liquid mass transfer in azeotropic systems. In particular, they indicate that the enrichment of one component affects the mass transfer of that component through the system, while it does not

significantly affect the mass transfer of other components in the system.

The results from this work complement and confirm the findings obtained earlier by our group from both stationary and non-stationary NEMD simulations of mass transfer.^{27,28} The simulation method developed in Ref. 28 provides detailed information on the mass transfer phenomena at vapor–liquid interfaces. Despite the simplicity of the mixtures investigated here, a wealth of effects and phenomena were observed. Yet, it is challenging to attribute the different phenomena to specific interfacial properties as they are intertwined in a complex way. Hence, many open questions in the field of mass transfer across fluid interfaces remain to be resolved. The simulation method developed in Ref. 28 and applied in this work provides a promising tool for such studies.

SUPPLEMENTARY MATERIAL

The supplementary material contains additional information about the simulation settings, the definition of interfacial properties, the results for the temperature dependence of mixtures B and C,

the composition dependence of the properties in the MVs for mixture A, as well as the profiles of flux and density at temperatures $T = 0.660 \epsilon k_B^{-1}$, $T = 0.770 \epsilon k_B^{-1}$, and $T = 0.825 \epsilon k_B^{-1}$ for all mixtures. In addition, the properties in the MVs for the simulations starting from the pure systems are shown in relation to their respective phase diagrams for all mixtures.

ACKNOWLEDGMENTS

The authors gratefully acknowledge funding for the present work by the ERC Advanced Grant ENRICO (Grant Agreement No. 694807) and by the Federal Ministry of Education and Research (BMBF, Germany) Grant No. 16ME0613 WindHPC. The authors gratefully acknowledge the support of Kai-Henrik Müller for carrying out simulations. The present work was conducted under the auspices of the Boltzmann-Zuse Society of Computational Molecular Engineering (BZS), and the simulations were carried out at the Regional University Computing Center Kaiserslautern (RHRK) under Grant No. RPTU-MTD as well as MOGON at Mainz.

AUTHOR DECLARATIONS

Conflict of Interest

The authors have no conflicts to disclose.

Author Contributions

Vilde Bråten: Data curation (equal); Formal analysis (lead); Investigation (lead); Methodology (equal); Visualization (lead); Writing – original draft (lead); Writing – review & editing (equal).
Dominik Schaefer: Data curation (equal); Investigation (equal).
Simon Stephan: Conceptualization (lead); Formal analysis (equal); Funding acquisition (equal); Methodology (lead); Resources (lead); Writing – review & editing (lead).
Hans Hasse: Funding acquisition (equal); Methodology (equal); Writing – review & editing (equal).

DATA AVAILABILITY

The data that support the findings of this study are available from the corresponding author upon reasonable request.

REFERENCES

- 1 M. Horsch, J. Vrabec, M. Bernreuther, S. Grottel, G. Reina, A. Wix, K. Schaber, and H. Hasse, “Homogeneous nucleation in supersaturated vapors of methane, ethane, and carbon dioxide predicted by brute force molecular dynamics,” *J. Chem. Phys.* **128**, 164510 (2008).
- 2 J. Vrabec, M. Horsch, and H. Hasse, “Molecular dynamics based analysis of nucleation and surface energy of droplets in supersaturated vapors of methane and ethane,” *J. Heat Transfer* **131**, 043202 (2009).
- 3 J. W. Cahn, “Critical point wetting,” *J. Chem. Phys.* **66**, 3667–3672 (1977).
- 4 M. Heier, S. Stephan, F. Diewald, R. Müller, K. Langenbach, and H. Hasse, “Molecular dynamics study of wetting and adsorption of binary mixtures of the Lennard-Jones truncated and shifted fluid on a planar wall,” *Langmuir* **37**, 7405–7419 (2021).
- 5 M. T. Rauter, A. Aasen, S. Kjelstrup, and Ø. Wilhelmsen, “A comparative study of experiments and theories on steady-state evaporation of water,” *Chem. Thermodyn. Therm. Anal.* **8**, 100091 (2022).

- 6 A. Lotfi, J. Vrabec, and J. Fischer, “Evaporation from a free liquid surface,” *Int. J. Heat Mass Transfer* **73**, 303–317 (2014).
- 7 K. Kashefi, L. M. Pereira, A. Chapoy, R. Burgass, and B. Tohidi, “Measurement and modelling of interfacial tension in methane/water and methane/brine systems at reservoir conditions,” *Fluid Phase Equilib.* **409**, 301–311 (2016).
- 8 Y. Liu, H. A. Li, and R. Okuno, “Measurements and modeling of interfacial tension for CO₂/CH₄/brine systems under reservoir conditions,” *Ind. Eng. Chem. Res.* **55**, 12358–12375 (2016).
- 9 W. Li and Z. Jin, “Molecular dynamics simulations of natural gas-water interfacial tensions over wide range of pressures,” *Fuel* **236**, 480–492 (2019).
- 10 F. Llovel, N. Mac Dowell, F. J. Blas, A. Galindo, and G. Jackson, “Application of the SAFT-VR density functional theory to the prediction of the interfacial properties of mixtures of relevance to reservoir engineering,” *Fluid Phase Equilib.* **336**, 137–150 (2012).
- 11 G. Niño-Amézquita, D. van Putten, and S. Enders, “Phase equilibrium and interfacial properties of water + CO₂ mixtures,” *Fluid Phase Equilib.* **332**, 40–47 (2012).
- 12 A. Silvestri, S. L. S. Stipp, and M. P. Andersson, “Predicting CO₂-H₂O interfacial tension using COSMO-RS,” *J. Chem. Theory Comput.* **13**, 804–810 (2017).
- 13 S. Enders and H. Kahl, “Interfacial properties of water+alcohol mixtures,” *Fluid Phase Equilib.* **263**, 160–167 (2008).
- 14 O. G. Niño-Amézquita and S. Enders, “Phase equilibrium and interfacial properties of water+methane mixtures,” *Fluid Phase Equilib.* **407**, 143–151 (2016).
- 15 S. Stephan and H. Hasse, “Interfacial properties of binary mixtures of simple fluids and their relation to the phase diagram,” *Phys. Chem. Chem. Phys.* **22**, 12544–12564 (2020).
- 16 S. Stephan and H. Hasse, “Influence of dispersive long-range interactions on properties of vapour-liquid equilibria and interfaces of binary Lennard-Jones mixtures,” *Mol. Phys.* **118**, e1699185 (2020).
- 17 A. H. Falls, L. E. Scriven, and H. T. Davis, “Adsorption, structure, and stress in binary interfaces,” *J. Chem. Phys.* **78**, 7300–7317 (1983).
- 18 S. Becker, S. Werth, M. Horsch, K. Langenbach, and H. Hasse, “Interfacial tension and adsorption in the binary system ethanol and carbon dioxide: Experiments, molecular simulation and density gradient theory,” *Fluid Phase Equilib.* **427**, 476–487 (2016).
- 19 S. Stephan, K. Langenbach, and H. Hasse, “Enrichment of components at vapour-liquid interfaces: A study by molecular simulation and density gradient theory,” *Chem. Eng. Trans.* **69**, 295–300 (2018).
- 20 S. Stephan, K. Langenbach, and H. Hasse, “Interfacial properties of binary Lennard-Jones mixtures by molecular simulation and density gradient theory,” *J. Chem. Phys.* **150**, 174704 (2019).
- 21 S. Stephan and H. Hasse, “Enrichment at vapour-liquid interfaces of mixtures: Establishing a link between nanoscopic and macroscopic properties,” *Int. Rev. Phys. Chem.* **39**, 319–349 (2020).
- 22 S. Stephan, H. Cárdenas, A. Mejía, and E. A. Müller, “The monotonicity behavior of density profiles at vapor-liquid interfaces of mixtures,” *Fluid Phase Equilib.* **564**, 113596 (2023).
- 23 I. Nitzke, R. Stierle, S. Stephan, M. Pfitzner, J. Gross, and J. Vrabec, “Phase equilibria and interface properties of hydrocarbon propellant-oxygen mixtures in the transcritical regime,” *Phys. Fluids* **35**, 032117 (2023).
- 24 C. Klink and J. Gross, “A density functional theory for vapor-liquid interfaces of mixtures using the perturbed-chain polar statistical associating fluid theory equation of state,” *Ind. Eng. Chem. Res.* **53**, 6169–6178 (2014).
- 25 J. M. Garrido, M. M. Piñeiro, A. Mejía, and F. J. Blas, “Understanding the interfacial behavior in isopycnic Lennard-Jones mixtures by computer simulations,” *Phys. Chem. Chem. Phys.* **18**, 1114–1124 (2016).
- 26 R. Nagl, P. Zimmermann, and T. Zeiner, “Interfacial mass transfer in water-toluene systems,” *J. Chem. Eng. Data* **65**, 328–336 (2020).
- 27 S. Stephan, D. Schaefer, K. Langenbach, and H. Hasse, “Mass transfer through vapour-liquid interfaces: A molecular dynamics simulation study,” *Mol. Phys.* **119**, e1810798 (2021).
- 28 D. Schaefer, S. Stephan, K. Langenbach, M. T. Horsch, and H. Hasse, “Mass transfer through vapor-liquid interfaces studied by non-stationary molecular dynamics simulations,” *J. Phys. Chem. B* **127**, 2521–2533 (2023).

- ²⁹S. Stephan and H. Hasse, “Molecular interactions at vapor-liquid interfaces: Binary mixtures of simple fluids,” *Phys. Rev. E* **101**, 012802 (2020).
- ³⁰J. Staubach and S. Stephan, “Interfacial properties of binary azeotropic mixtures of simple fluids: Molecular dynamics simulation and density gradient theory,” *J. Chem. Phys.* **157**, 124702 (2022).
- ³¹J. S. Rowlinson and F. L. Swinton, *Liquids and Liquid Mixtures* (Butterworth, 1982).
- ³²E. Schäfer, C. Vogelpohl, G. Sadowski, and S. Enders, “Simultane modellierung von phasengleichgewichten und grenzflächeneigenschaften mithilfe des PCP-SAFT-modells,” *Chem. Ing. Tech.* **85**, 1512–1522 (2013).
- ³³C. Niethammer, S. Becker, M. Bernreuther, M. Buchholz, W. Eckhardt, A. Heinicke, S. Werth, H.-J. Bungartz, C. W. Glass, H. Hasse, J. Vrabc, and M. Horsch, “*Is1 mardyn*: The massively parallel molecular dynamics code for large systems,” *J. Chem. Theory Comput.* **10**, 4455–4464 (2014).
- ³⁴C. Braga, J. Muscatello, G. Lau, E. A. Müller, and G. Jackson, “Nonequilibrium study of the intrinsic free-energy profile across a liquid-vapour interface,” *J. Chem. Phys.* **144**, 044703 (2016).
- ³⁵L. Casalino, Z. Gaieb, J. A. Goldsmith, C. K. Hjorth, A. C. Dommer, A. M. Harbison, C. A. Fogarty, E. P. Barros, B. C. Taylor, J. S. McLellan, E. Fadda, and R. E. Amaro, “Beyond shielding: The roles of glycans in the SARS-CoV-2 spike protein,” *ACS Cent. Sci.* **6**, 1722–1734 (2020).
- ³⁶S. Stephan, M. Dyga, I. Alabd Alhafez, J. Lenhard, H. M. Urbassek, and H. Hasse, “Reproducibility of atomistic friction computer experiments: A molecular dynamics simulation study,” *Mol. Simul.* **47**, 1509–1521 (2021).
- ³⁷M. P. Allen and D. J. Tidesely, *Computer Simulations of Liquids* (Oxford University Press, Inc., 1987).
- ³⁸H. A. Lorentz, “Ueber die anwendung des satzes vom virial in der kinetischen theorie der gase,” *Ann. Phys.* **248**, 127–136 (1881).
- ³⁹D. Berthelot, “Sur le mélange des gaz,” *C. R. Hebd. Seances Acad. Sci.* **126**, 1703–1706 (1898).
- ⁴⁰M. Heier, S. Stephan, J. Liu, W. G. Chapman, H. Hasse, and K. Langenbach, “Equation of state for the Lennard-Jones truncated and shifted fluid with a cut-off radius of 2.5σ based on perturbation theory and its applications to interfacial thermodynamics,” *Mol. Phys.* **116**, 2083–2094 (2018).
- ⁴¹D. Fertig, H. Hasse, and S. Stephan, “Transport properties of binary Lennard-Jones mixtures: Insights from entropy scaling and conformal solution theory,” *J. Mol. Liq.* **367**, 120401 (2022).
- ⁴²D. Fertig and S. Stephan, “Influence of dispersive long-range interactions on transport and excess properties of simple mixtures,” *Mol. Phys.* (published online) (2023).
- ⁴³S. Stephan, J. Liu, K. Langenbach, W. G. Chapman, and H. Hasse, “Vapor–liquid interface of the Lennard-Jones truncated and shifted fluid: Comparison of molecular simulation, density gradient theory, and density functional theory,” *J. Phys. Chem. C* **122**, 24705–24715 (2018).
- ⁴⁴K. Shi, E. R. Smith, E. E. Santiso, and K. E. Gubbins, “A perspective on the microscopic pressure (stress) tensor: History, current understanding, and future challenges,” *J. Chem. Phys.* **158**, 040901 (2023).